Ahmad R. Gharaibeh[1]
Department of Mechanical Engineering,
ES2 Center,
Binghamton University-SUNY,
Binghamton, NY 13902
e-mail: agharai1@binghamton.edu

Yaman M. Manaserh
Department of Mechanical Engineering,
ES2 Center,
Binghamton University-SUNY,
Binghamton, NY 13902

Mohammad I. Tradat
Department of Mechanical Engineering,
ES2 Center,
Binghamton University-SUNY,
Binghamton, NY 13902

Firas W. AlShatnawi
Department of Systems Science and
Industrial Engineering,
CAMM Center,
Binghamton University-SUNY,
Binghamton, NY 13902

Scott N. Schiffres
Department of Mechanical Engineering,
ES2 Center,
Binghamton University-SUNY,
Binghamton, NY 13902

Bahgat G. Sammakia
Department of Mechanical Engineering,
ES2 Center,
Binghamton University-SUNY,
Binghamton, NY 13902

Using a Multi-Inlet/Outlet Manifold to Improve Heat Transfer and Flow Distribution of a Pin Fin Heat Sink

The increased power consumption and continued miniaturization of high-powered electronic components have presented many challenges to their thermal management. To improve the efficiency and reliability of these devices, the high amount of heat that they generate must be properly removed. In this paper, a three-dimensional numerical model has been developed and experimentally validated for several manifold heat sink designs. The goal was to enhance the heat sink's thermal performance while reducing the required pumping power by lowering the pressure drop across the heat sink. The considered designs were benchmarked to a commercially available heat sink in terms of their thermal and hydraulic performances. The proposed manifolds were designed to distribute fluid through alternating inlet and outlet branched internal channels. It was found that using the manifold design with 3 channels reduced the thermal resistance from 0.061 to 0.054 °C/W with a pressure drop reduction of 0.77 kPa from the commercial cold plate. A geometric parametric study was performed to investigate the effect of the manifold's internal channel width on the thermohydraulic performance of the proposed designs. It was found that the thermal resistance decreased as the manifold's channel width decreased, up until a certain width value, below which the thermal resistance started to increase while maintaining low-pressure drop values. Where the thermal resistance significantly decreased in the 7 channels design by 16.4% and maintained a lower pressure drop value below 0.6 kPa. [DOI: 10.1115/1.4054461]

Keywords: electronics cooling, manifold, heat sink, thermal resistance, numerical simulation

1 Introduction

Digital data from various regions of the internet, like social media networks, blogs, e-commerce, artificial intelligence, and quantum computing, has continued to rise worldwide [1]. This enormous amount of data, which must be recorded, routed, stored, assessed, and retrieved, is overwhelming data centers [2]. The increased demand for data center services is inevitably accompanied by an abrupt increase in their energy usage. The overall data center's energy consumption was estimated to account for roughly 1.31% of worldwide annual energy usage in 2012 [3], with their cooling systems responsible for up to half of their energy consumption [4]. Accordingly, the search for energy-efficient improvements to data centers is increasing.

Moreover, advances in the manufacturing of chips and other integrated components accompanied by the increasing demand for data processing have resulted in a rise of power densities and heat dissipation. More than 90% of today's data centers still use air-cooling technologies to dissipate the heat generated by their IT equipment [5]. However, it has become clear that air-cooling technologies are reaching their reticle limits. They suffer from multiple drawbacks that prevent them from coping with chip's high heat flux, including large thermal resistances that lead to so-called "dark silicon" and bulky heatsinks [6–8]. In response, new and improved cooling methods have been developed that can be implemented standalone or alongside traditional air-cooling technologies. Such as indirect single- or two-phase liquid cooling and single- or two-phase immersion cooling [9–16]. Cooling high heat flux electronics using single-phase liquid cooling technologies has proven to be an effective, practical, and energy-efficient technique [17–20].

Tuckerman and Pease [17] proposed the first traditional single-phase liquid-cooled microchannel heat sink. A $10 \times 10\,\text{mm}^2$ silicon heat sink was fabricated with a $790\,\text{W/cm}^2$ power density, and it was experimentally tested using water as the coolant. The authors accomplished a thermal resistance of 0.09 °C/W and a pressure drop of 186 kPa. Ndao [21] experimentally studied the effects of pin fin structure and crossflow area on the heat transfer coefficients of single-phase impingement pointed on micropin fins (MPF). They found that crossflow did not have a substantial impact on the heat transfer coefficient. While area improvement, on the other hand, was found to play a crucial role in the enhancement of overall heat transfer. Gupta [22] studied the hydrodynamic and heat transfer characteristics of different shapes of perforated micropin-fin heat sinks with various numbers of perforations. Siu [23] conducted an experiment with liquid single-phase flow to determine the heat transfer coefficient and pressure drop of a square MPF heat sink, and compared the experimental results to an existing correlation that predicts the results with particular ranges of Reynolds number. Ahmadian [24] applied the finite volume method (FVM) to investigate the effect of

[1]Corresponding author.

Contributed by the Electronic and Photonic Packaging Division of ASME for publication in the Journal of Electronic Packaging. Manuscript received November 23, 2021; final manuscript received April 25, 2022; published online May 19, 2022. Assoc. Editor: Ercan Dede.

optimizing the geometric parameters of pin-fin heat sinks and the impact of pin-fin shape on the heat sink thermohydraulic performance. Li [25] numerically studied the flow and convective heat transfer of channels in novel microchannel heat sink designs. The authors studied and analyzed the impact of the cavities and fins combined on the hydraulic and thermal characteristics, the heat sinks' thermodynamic performances, and the impact of fin configuration on total performance. Hasan [26] numerically investigated MPF heat sinks with different geometries as well as an unfinned microchannel heat sink. They used pure water, diamond-water nanofluid, and Al_2O_3-water nanofluid as cooling fluids. Ahmed [27] studied the geometrical parameters and the shape of the grooved microchannels in an aluminum heat sink. The optimum design was obtained by using the FVM to solve the governing and energy equations. The best heat sink design enhanced the Nusselt number and the friction factor by 51.5% and 2.35%, respectively. Using a single-phase liquid cooling technique, Wan [28] investigated the effect of pin-fin dimensions on the thermal and hydraulic performance of pin-fin microgaps. The author found that the circular pin-fin array has superior thermal characteristics than the square pin-fin array and that it also had a lower pressure drop. Chiu [29] studied experimentally and numerically the effects of geometric parameters, such as porosity and pin-fin diameter, on the heat transfer characteristics and hydraulic performance of an aluminum MPF heat sink. Wiriyasart [30] used nanofluids and water as coolants to investigate the thermal and hydraulic performance of liquid impingement on heat sink with several fin configurations. These studies primarily focused on assessing and optimizing a heat sink's fins, disregarding the manifold and the method of fluid distribution through the channels of the heat sink.

Just a few studies have concentrated on investigating the influence of the manifold and its shape on the heat sink's thermal and hydraulic performance. Ryu [31] carried out a three-dimensional numerical simulation and investigated the sensitivity of design parameters to improve the manifold microchannel thermal and hydraulic performance. Boteler [32] used computational analysis to study the impact of manifold microchannel width, microchannel fin, and chip length of a manifold microchannel cooler heat exchanger. Whitt [33] performed a design optimization study using computational fluid dynamics (CFD) to analyze the effect of manifold shape and nozzles on the thermo-hydraulic characteristics of a nonmetallic three-dimensional (3D) printed heat spreader with direct jet impingement. Zhou [34] designed a microchannel heat sink and manifold with impingement and collection slots for three different inverter power modules. The cold plate performance was evaluated using CFD software. Solovitz [35] numerically analyzed a multichannel manifold and analytically estimated the pressure drops along each possible flow path. A package level of 3D printed manifold was designed and characterized experimentally by Wei [36] using direct jet impingement. Gonzalez-Valle [37] experimentally investigated a hybrid water-cooled heat sink that contained a copper plate and a 3D printed manifold. In addition, they investigated the impact of jet nozzle distribution, the number of jets, the flood chamber's depth, and an enhancement to the copper plate on the characteristics of heat transfer and fluid flow. Jung [38] conducted an experimental study on the thermal performance of a 3D printed manifold attached to an embedded silicon microchannel heat sink using single-phase R-245fa as a coolant. The author achieved 0.15 cm^2-° C/W thermal resistance with a 28.7 kPa pressure drop. In a later study [39], the authors extended their investigation to include a parametric study of reducing chip thickness, channel width, and changing the geometry of the 3D manifold channels. They used CFD and water instead of R-245fa as a coolant. Zhou [40] designed a hierarchical manifold microchannel that has a U-type flow arrangement and compared it with a typical manifold microchannel experimentally and numerically in terms of thermal performance and fluid flow. Luo [41] performed a computational analysis on several manifold arrangements and investigated flow maldistribution in single-phase flow and thermohydraulic characteristics in two-phase flow for (Z-shaped, C-shaped, H-shaped, and U-shaped) manifolds. Zhou [42] designed a modular manifold with several micro/mini channel heat sink topologies that can be established in parallel, series, or mixed parallel and series to achieve uniform cooling for each module. The thermal and hydraulic performance of each configuration were investigated numerically using CFD software. Gilmore [43] developed a three-dimensional numerical model for heat transfer in an open manifold microchannel. Pressure drops of up to 75% were achieved in the microchannel model with negligible change to thermal resistance, and pressure drops of up to 25% were achieved in the manifold model with up to a 21% increase in the thermal resistance. There are just a few research studies that discuss the effect of manifold design, which indicates that any new manifold design proposals will significantly contribute to the current body of literature.

This study presents a new manifold design concept that can be easily manufactured and adapted to various heat sink geometries. It was devised to overcome the large pressure drops needed for pushing fluid through narrow heat sink channels, which is a significant barrier to removing large heat fluxes. By design, the manifold passively distributes flow through the heat sink with minimal pressure drop, which results in a decreased thermal resistance. Additionally, it reduces the caloric resistance and total pressure drop across the heat sink. Other advantages of this design are that it reduces erosion-corrosion of the heat sink fins and improves the uniformity of flow distribution through the channels of the heat sink. These are achieved through a reduction of the fluid velocity, which occurs because the manifold splits the fluid into several internally branched channels, thereby shortening the flow path and allowing the fluid to absorb a significant amount of heat. To the best of the authors' knowledge, this concept has not yet been presented in the literature. Therefore, it is the author's hope that this work will open new avenues of research and draw attention to the study and design of functional manifolds as a means of improving the heat sinks' thermal and hydraulic performance. In addition, a geometric parametric study of channel width will be conducted to better understand how changing this parameter will affect a heat sink's thermal resistance and pressure drop.

2 Numerical Method

2.1 Heat Sink Model. This study characterized a 50 × 50 mm^2 commercially available heat sink consisting of two parts, as shown in Fig. 1. The first part was the metal base with a total of 729 square pin fins array made of copper. The second part was the manifold, which included a single impingement inlet and a single outlet made of plastic. The geometric dimensions of the heat sink were accurately obtained using a 3D surface profiler (Keyence laser scanning microscope VK-X1050), as shown in Fig. 1(*b*). This apparatus is a noncontact 3D surface profiler designed to use a laser beam to accurately scan a surface and capture high-quality images with high magnifications of up to 100×. Table 1 lists all the geometric dimensions of the heat sink.

2.2 Manifold Concept. The overall design of the manifold shape consisted of a single 10.9 mm diameter inlet and outlet port, which were branched into rectangular internal channels, as shown in Fig. 2. Several designs were considered in this study as seen in Fig. 3, each with a different number of branched internal channels. Depending on the number of channels, the internal channels could be connected in an alternating sequence to the inlet and outlet ports. With five total channels, the entering fluid can branch into three assigned inlet channels, impinge upon the pin fins of the heat sink, flow through the remaining two channels, and exit through the common outlet manifold port. Conversely, the entering fluid can branch into two assigned inlet channels, impinge upon the pin fins of the heat sink, flow through the remaining three channels, and exit through the common outlet manifold port. This kind of manifold could be 3D printed with smooth turns that

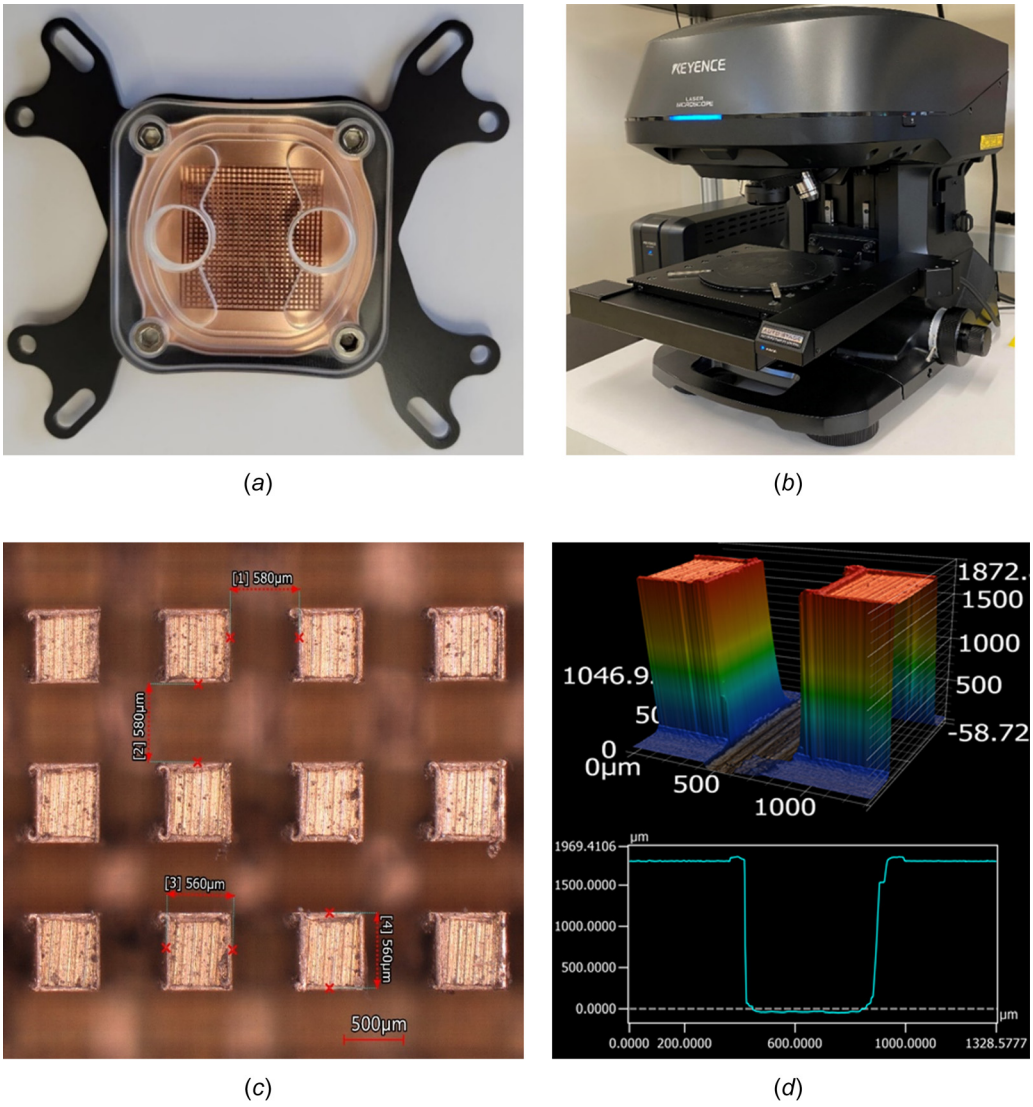

Fig. 1 (*a*) Commercial cold plate, (*b*) Keyence laser scanning microscope, (*c*) microscopic picture of the square pin fins, and (*d*) 3D and profile graph for the fin height

reduce pressure drop. The geometric parameters of the manifold are described in Table 2.

2.3 Governing Equations and Assumptions. All the simulations conducted in this investigation used 6SigmaET. The FVM was used in this commercial software package to discretize and solve the system of governing equations (Continuity, Navier–Stokes, and Energy) in the computational domain on a staggered grid. This finite volume algorithm has been specifically developed for the simulation of electronics cooling components. Therefore, it is feasible to use it to build accurate models for electronic cooling devices like heat sinks.

Table 1 Geometric parameters of the heat sink with their values

Parameter	Symbol	Value
Heat sink base length	L	50 mm
Heat sink base width	W	50 mm
Heat sink base thickness	T	3 mm
Fin height	h_F	1.8 mm
Fin width	w_F	0.56 mm
Channel width	w_{ch}	0.58 mm

The basic assumptions that were applied while solving the numerical models are as follows:

(1) The flow is three-dimensional, incompressible, and in a steady-state.
(2) The chip and heat sink is insulated; therefore, no heat is transferred to the surrounding either by radiation or free convection.
(3) The effects of wall roughness and gravity are negligible.
(4) Constant thermo-physical properties.
(5) Negligible effects of radiative and viscous heat transfer.

The continuity, momentum, and energy equations used in the software for solving the numerical model for fluid flow and heat transfer in liquid and solid states after applying the above assumptions are expressed as follows:

$$\nabla \cdot (\rho_f \mathbf{u}) = 0 \tag{1}$$

$$(\mathbf{u}.\nabla)\rho_f \mathbf{u} = -\nabla P + \mu_f \nabla^2 \mathbf{u} \tag{2}$$

$$\rho_f c_{\rho_f} (\mathbf{u}.\nabla) T_f = K_f \nabla^2 T_f \quad \text{(Liquid)} \tag{3}$$

$$k_S \nabla^2 T_S = 0 \quad \text{(Solid)} \tag{4}$$

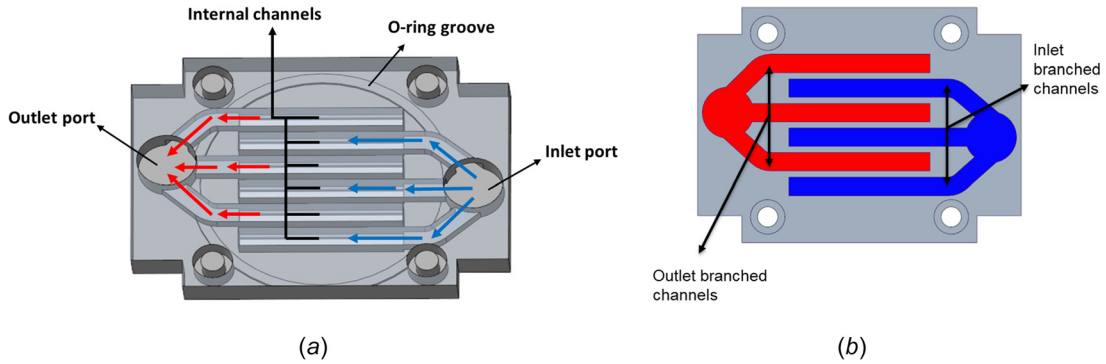

Fig. 2 One of the proposed designs of the manifold: (*a*) proposed manifold with 6 internal channels and (*b*) section view of the manifold with the internal channels

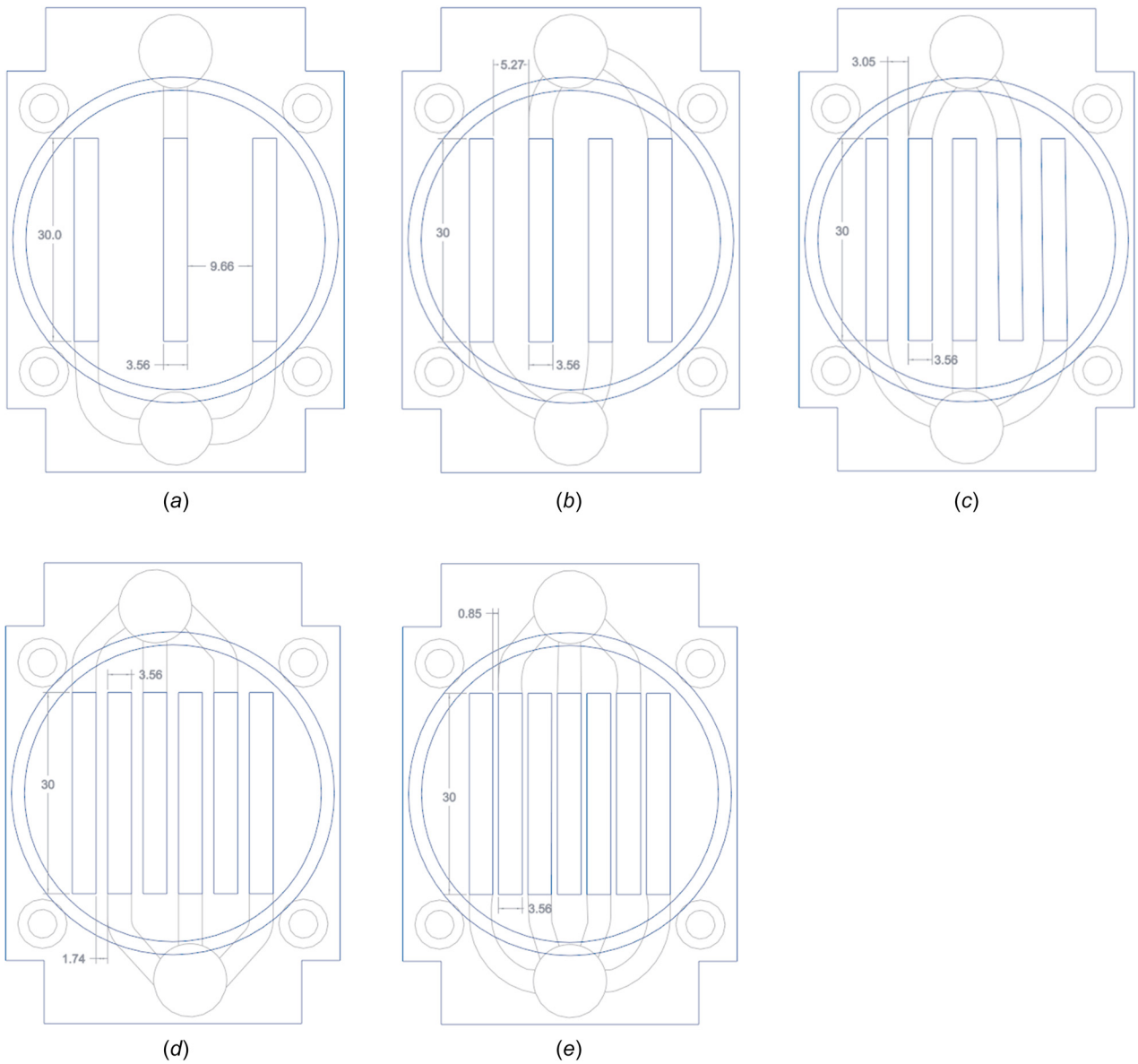

Fig. 3 Schematic of channels dimensions and layout for the proposed designs: (*a*) 3 channels, (*b*) 4 channels, (*c*) 5 channels, (*d*) 6 channels, and (*e*) 7 channels

Table 2 Geometric parameters of the manifold with their values

Parameter	Symbol	Value
Manifold width	W_m	50 mm
Manifold length	L_m	69 mm
Manifold height	H_m	18 mm
Common inlet port diameter	D_{in}	10.9 mm
Common outlet port diameter	D_{out}	10.9 mm
Internal channel width	$w_{m,\text{ch}}$	3.56 mm
Internal channel length	$l_{m,\text{ch}}$	30 mm

2.4 Grid Generation and Sensitivity Analysis (Numerical Model). The geometry of the manifold, copper plate, thermal interface material (TIM), and electronic chip was modeled using 6SigmaET and was considered as the computational domain, as shown in Fig. 4. However, the creation of a proper grid is essential to assuring reliability while developing a CFD model. Therefore, a structured grid with hexahedral cells, which ensured a high grid generation [44], was deployed over the computational domain. There was a higher grid concentration in the regions of high gradients associated with the proper boundary conditions. The boundary conditions used in the simulation are constant inlet flow rate, all the surrounding wall surfaces were assumed to be adiabatic and no-slip except for the bottom, where a constant heat flux was applied from a chip with a surface area of 6.45 cm^2, and constant pressure at the outlet. The thermal properties of the TIM were the same as the ones used in the experiment (Kryonaut). The working fluid used in the simulation was de-ionized water (DI) with a 32 °C inlet temperature. The thermo-physical properties of the liquid and solid phases used in the simulation are summarized in Table 3.

A computational grid is necessary to obtain a solution and is generated automatically by the software as it uses a unique multilevel, unstructured staggered grid solver. It provides an efficient and innovative technique to solve the governing equations required to provide an accurate simulation of heat and fluid flow. A high-resolution grid is laid across the whole model's design, followed by a series of progressively coarser cartesian grids. The smallest cells were 9.8, 7.5, 8×10^{-5} in the x, y, and z direction, respectively. The computational grid is used to discretize the equations used by the solver using the FVM, and finer grids (i.e., with a larger number of cells) generally give more accurate results. The unlimited grid was selected, which represents the number of cells beyond which any further refinement would not yield any appreciable difference in results. Then, the grid is more refined between heat sink channels to capture the flow field as seen in Fig. 4.

Table 3 Thermophysical properties of fluid and solids

	ρ (kg/m^3)	c_p (J/kg.°C)	k (W/m.°C)
Water	995.7	4183	0.5948
Copper	8978	381	387.6
Silicon	2329	705	149
TIM	3700	—	6.5

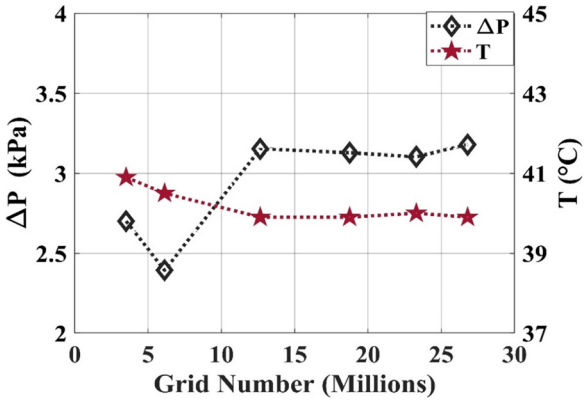

Fig. 5 Grid sensitivity results based on the maximum base temperature and pressure drop for the original heat sink

A grid sensitivity study was performed on the basis of the pressure drop and the maximum temperature at the base of the heat sink. It was found that the most suitable number of grids, for which there was minimal variation in the maximum base temperature and pressure drop, exceeded 18 million. The results of the grid sensitivity study are shown in Fig. 5. Note, throughout this work, the number of grid cells was adjusted to fit the different heat sink configurations.

2.5 Performance Evaluation Parameters. To compare different heat sink configurations, some response parameters must be considered and evaluated, such as hydraulic and thermal performance. Thermal resistance can be defined as the difference between the maximum base temperature ($T_{b,\text{max}}$) and the coolant inlet

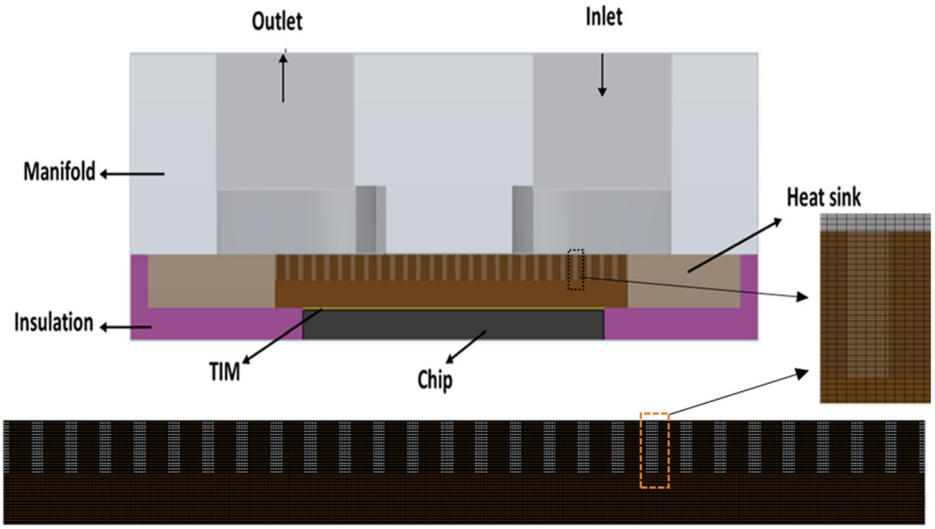

Fig. 4 Computational domain of the numerical model with cross-sectional view of the grid between channels

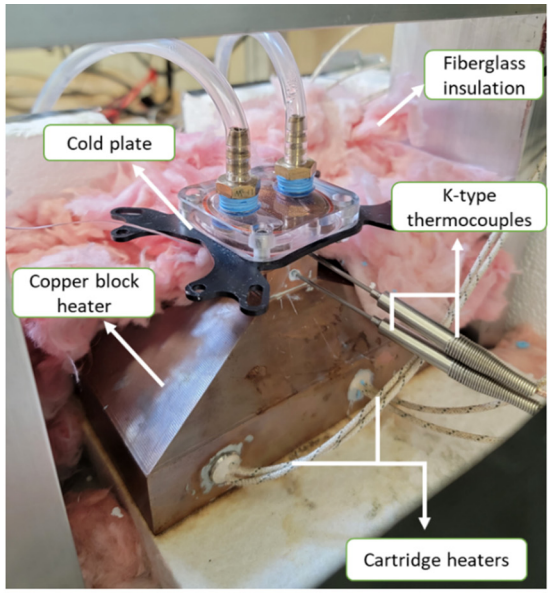

(*a*)

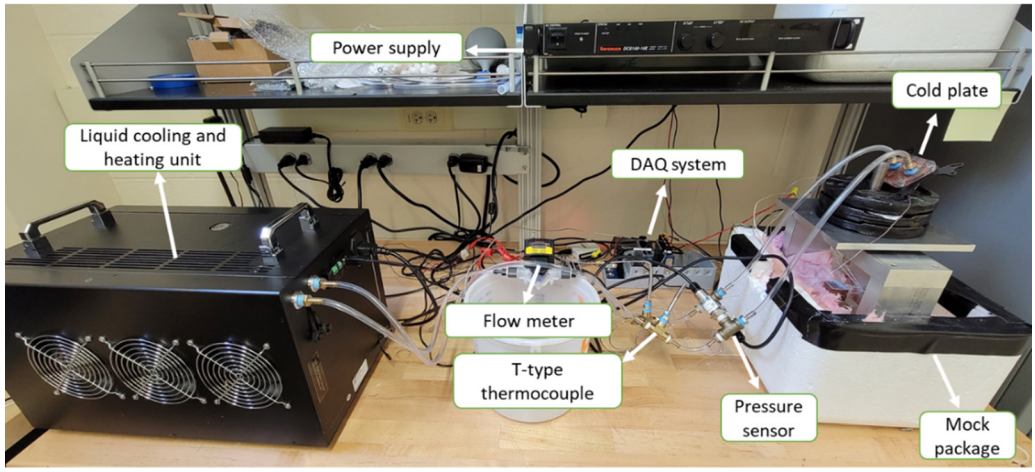

(*b*)

Fig. 6 Experimental rig used to validate the numerical methodology: (*a*) mock package including the copper block heater and the cold plate and (*b*) experimental setup

temperature (T_{in}), divided by the total power of the electronic chip (q), which is mathematically expressed as follows:

$$R_{\text{th}} = \frac{T_{b,\max} - T_{\text{in}}}{q} \tag{5}$$

Moreover, the coefficient of performance (COP) was introduced to evaluate the thermo-hydraulic performance of the heat sink. The COP is defined by the ratio of the heat picked up by the fluid ($\dot{m}\, c_p(T_{\text{out}} - T_{\text{in}})$) at various inlet coolant temperatures to the pumping power ($\Delta P \times Q$), and is mathematically defined as follows:

$$\text{COP} = \frac{\dot{m}\, c_p(T_{\text{out}} - T_{\text{in}})}{\Delta P \times Q} \tag{6}$$

2.6 Experimental Setup. In this study, the experimental test setup shown in Fig. 6 was built to validate the numerical models' results with real experimental data. A copper block heater with a top surface area of 6.45 cm^2 was utilized to mimic a real chip. Four cartridge heaters were installed into the copper block heater. Each cartridge heater is capable of delivering 400 watts. The input power of the mock heater can be modified by varying the power delivered to the cartridge heater using a DC power supply. To accurately calculate the delivered input power at the top surface of the used mock heater, two K—type thermocouples with a known distance between them were used for measuring the temperature gradient along the copper block. To ensure that most of the heat was picked up by the heat sink with minimal loss, the copper block was placed in a polystyrene box and all sides except for the top surface were insulated with fiberglass. To measure the base temperature of the heat sink, two T-type thermocouples were installed in two machined slots at the bottom of the heat sink.

Omega PX309050A5V sensors and T-type thermocouples were used for the coolant pressure and temperature measurements at the inlet and outlet. During the experiment, thermal insulation was put around the pipes to prevent any heat losses. The flow rate and inlet temperature of the coolant were controlled by the ALH-2000 cooling distribution unit with a cooling capacity up to 2000 W, and a FTB314D flowmeter was used to monitor the coolant flow rate. The experimental data were collected by the National

Table 4 Specifications of experimental apparatus

Apparatus	Specification
Cooling distribution unit	ALH-2000 (cooling capacity 2000 W)
Flow sensor	Omega FTB314D (full scale accuracy: ±6%)
Pressure transducer	Omega PX309050A5V (accuracy ±0.8 kPa)
Thermocouples	T-type (accuracy: ±1 °C) K-type (accuracy: ±2.2 °C)

Instrument data acquisition system and was recorded using LABVIEW. Table 4 provides the specifications of the experimental apparatus.

3 Results and Discussion

3.1 Validation. An experiment was conducted at the specified boundary conditions to verify the numerical models used in the simulation in terms of pressure drop and base maximum temperature. DI water was used as the working fluid with a 32 °C inlet temperature. The total delivered power from the copper block to the heat sink was

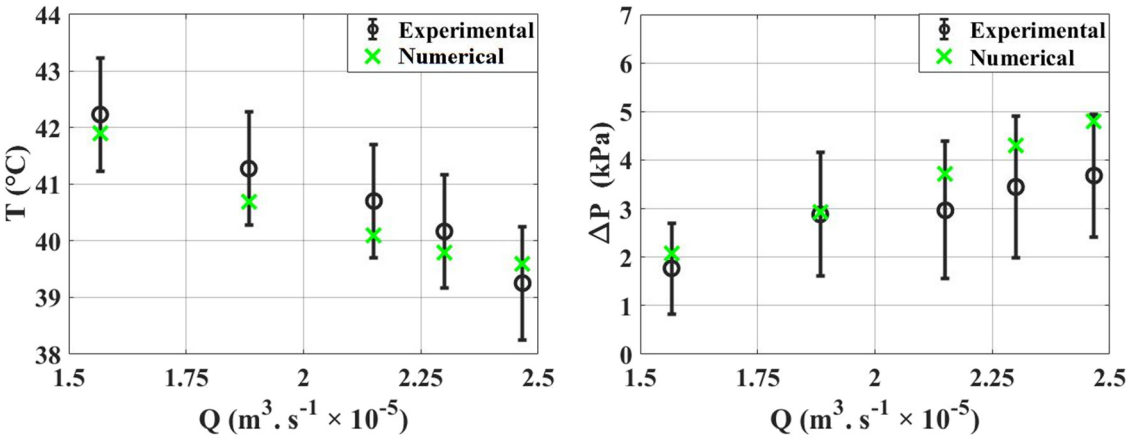

(*a*) (*b*)

Fig. 7 Numerical results validation with the experimental results: (*a*) temperature validation and (*b*) pressure drop validation

Table 5 Evaluated performance parameters for the baseline and proposed designs

Design	No. of inlets	No. of outlets	Flow rate (m^3/s) $\times 10^{-5}$	T_{avg} (°C)	$T_{b,max}$ (°C)	R_{th} (°C/W)	ΔP (kPa)	COP (10^3)
Baseline	1	1	1.6667	47.8	56.4	0.061	2.23	10.8
3 internal channels	1	2	1.6667	48.1	53.9	0.054	1.46	16.4
3 internal channels	2	1	1.6667	48.2	56.1	0.06	1.36	17.7
4 internal channels	2	2	1.6667	49.1	56.9	0.062	0.719	33.4
5 internal channels	2	3	1.6667	49.4	57	0.062	0.49	49
5 internal channels	3	2	1.6667	48.9	55.9	0.059	0.427	56.2
6 internal channels	3	3	1.6667	49.9	57.2	0.063	0.335	71.6
7 internal channels	3	4	1.6667	51.3	60.1	0.07	0.218	110
7 internal channels	4	3	1.6667	51.3	59.9	0.068	0.219	109.6

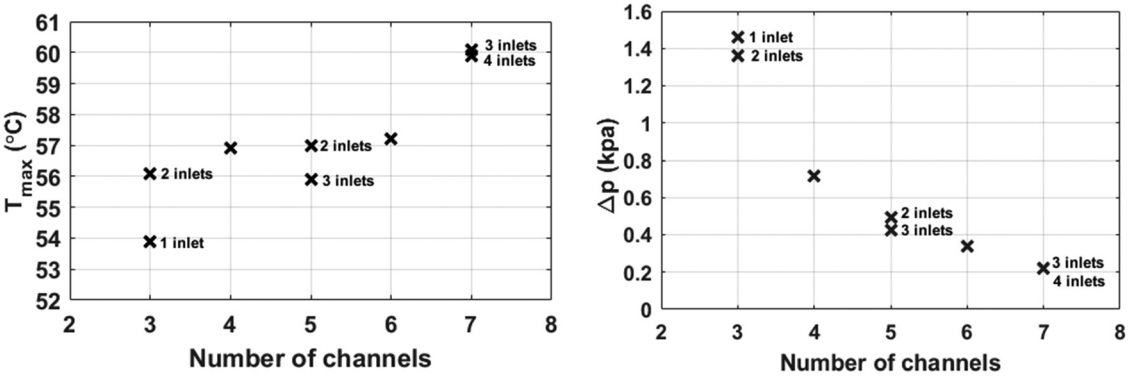

(*a*) (*b*)

Fig. 8 Maximum temperature and pressure drop relation with channels number: (*a*) maximum temperature as a function of channels number and (*b*) pressure drop as a function of channels number

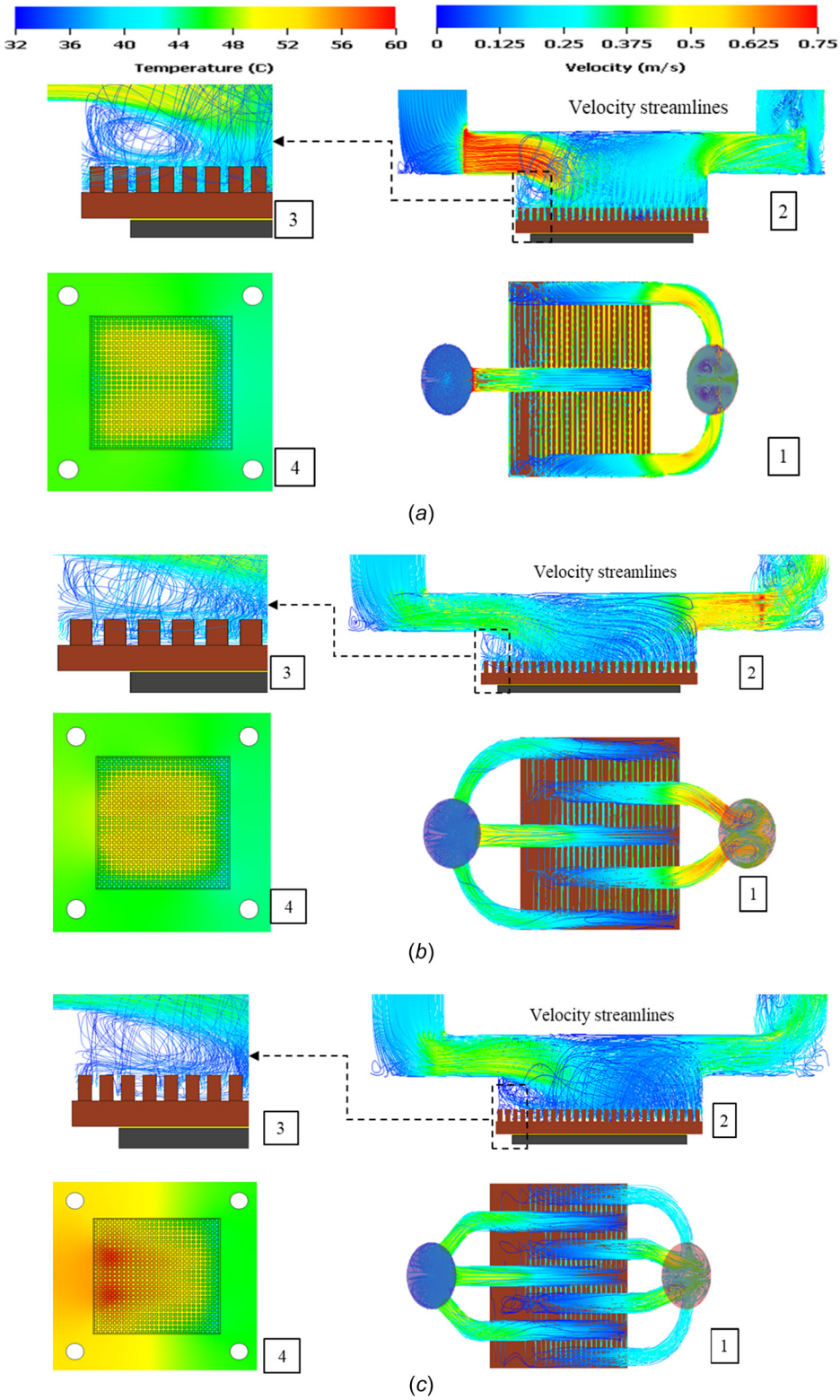

Fig. 9 Streamlines colored by velocity and temperature contours for best, worst and intermediate manifold designs: (*a*) 3 channels, 1 inlet, (*b*) 5 channels, 3 inlets, (*c*) 7 channels, 3 inlets. (counterclockwise from 1 to 4) 1: top view of velocity streamlines. 2: side view of velocity streamlines. 3: zoomed in side view of velocity streamlines (good and poor fluid penetration). 4: top view of heat sink temperature contours.

155 W. The experiment was conducted by varying the flow rate from 1.63×10^{-5} to 2.46×10^{-5} m^3/s (0.98–1.48 LPM).

Figure 7 compares the experimental and numerical results. The figure shows that the largest discrepancy in the base maximum temperature was less than the thermocouple's uncertainty. For the pressure drop recorded across the heat sink, the measured pressure drop from the experiment was first obtained for the system without the heat sink, including the fittings, by looping the inlet and outlet sides together. Then, during the experiment, the heat sink was included and the pressure drop of the heat sink was calculated

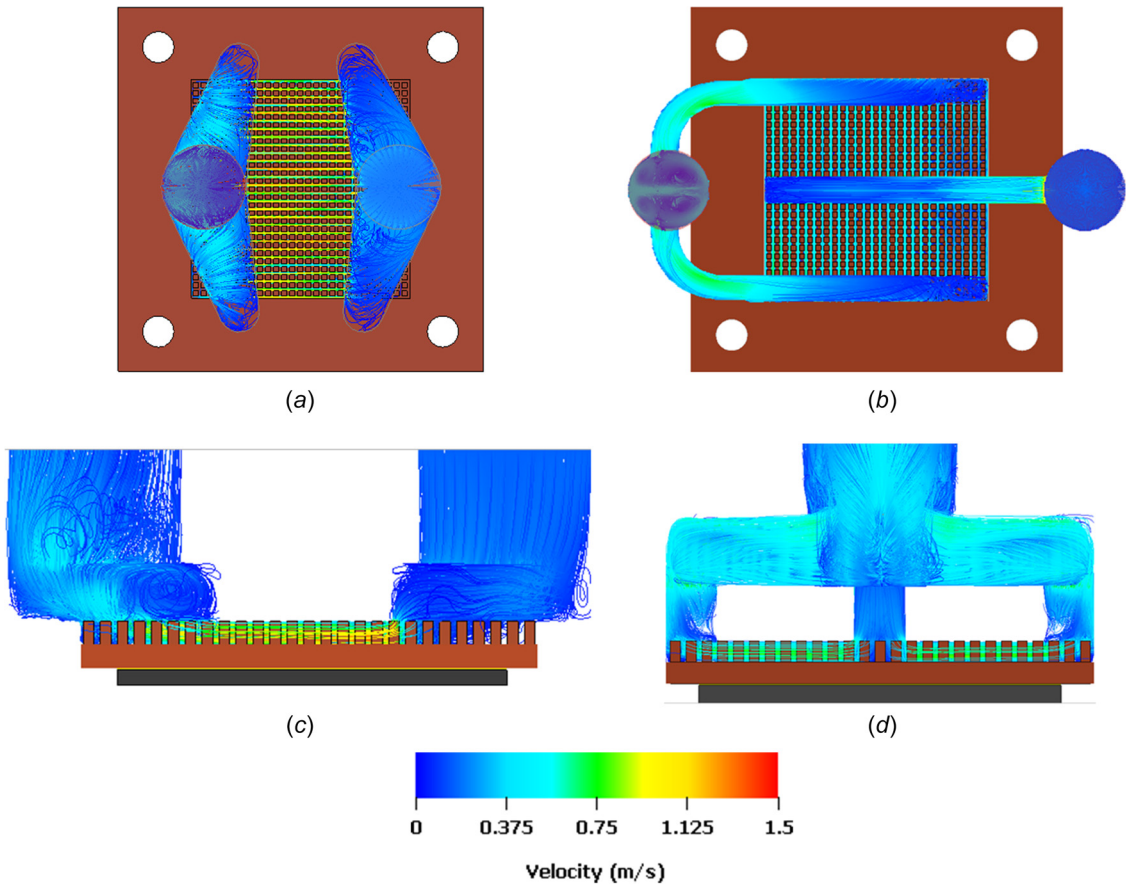

Fig. 10 Fluid flow streamlines in term of velocity for: (*a*) baseline design, (*b*) 3 internal channels design, (*c*) side view for the flow in the baseline design, and (*d*) side view for the flow in the 3 internal channels design

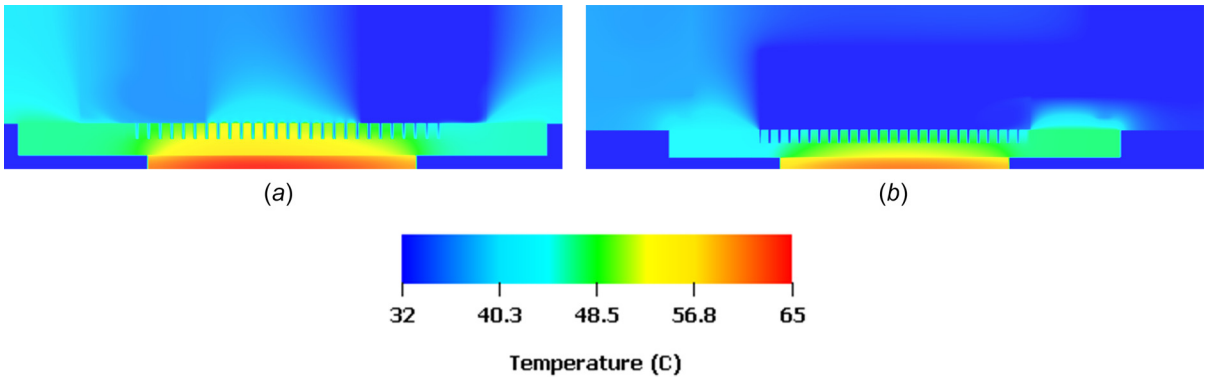

Fig. 11 Temperature contours at the computational domain center for: (*a*) baseline design and (*b*) 3 internal channels design

by subtracting the pressure drop readings with the heat sink from the pressure drop of the looped system. In this case, we have the measured pressure drop of the heat sink. From Fig. 7(*b*) it can be seen that the numerical results were within one standard deviation of the experimental readings, which shows great consistency.

The numerical model's accuracy was validated by the high degree of agreement between the numerical and experimental results. Based on this, the study proceeded with confidence in its findings as it considered alternative designs.

3.2 Baseline Case Versus Proposed Concept. One of the most important factors to consider when evaluating the heat sink's overall performance is the pumping power. Thus, to have an efficient heat sink that can remove large amounts of heat with the least amount of pumping power, several manifold designs with different numbers of internally branched channels were introduced and investigated. The number of internal channels varied from 3 to 7 in total. A detailed comparison was made of the baseline and alternative designs to better understand the advantages of the branched internal channel configuration.

The manifold's geometric parameters were identical for each design and the inlet/outlet ports have the same geometrical structure as the baseline design. The width and length of each internal channel were set to 3.56 mm and 30 mm, respectively. All designs functioned under the same simulated operating conditions. Table 5 summarizes the findings of the comparative study while incorporating the response parameters presented in an earlier section.

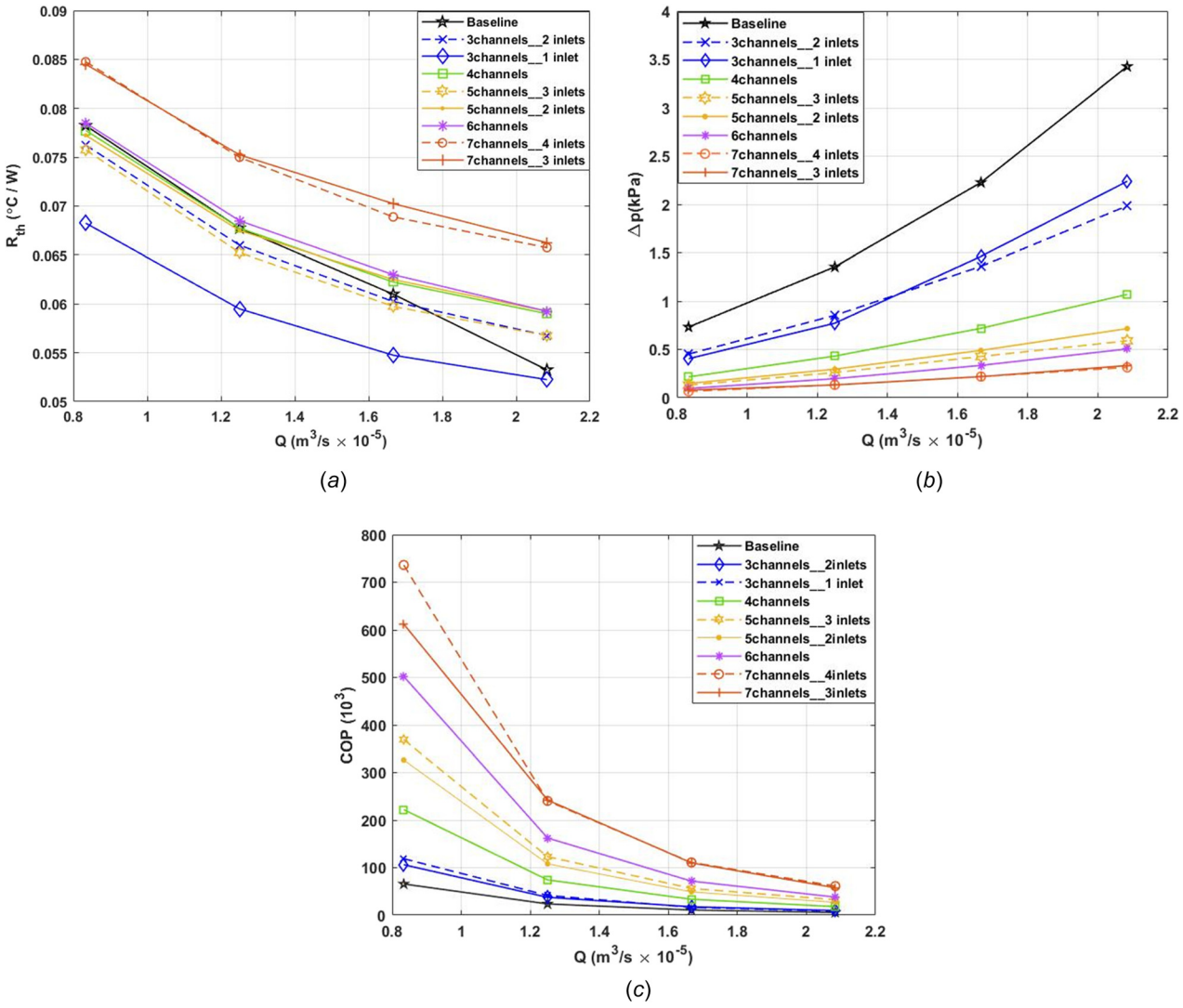

Fig. 12 (*a*) Thermal resistance, (*b*) pressure drop variation, and (*c*) coefficient of performance comparison for the baseline and the proposed designs at different flow rates

Using multiple inlets and outlets decreases the thermal resistance by reducing the caloric thermal resistance and pressure drop over the heat sink. First, dividing the flow into several inlets instead of a single inlet decreases the flow speed in these inlets dramatically. Second, this arrangement reduces the total distance traveled by the coolant inside the heat sink by shortening the route between the inlets and outlets.

When comparing the baseline design with the proposed designs at the same delivered flow rate of 1 LPM, it was found that the design with 3 total internal channels, comprised of 1 inlet channel and 2 outlet channels, reduced the thermal resistance by 11.5%. This reduced the necessary pumping power and hence saved more energy by reducing the pressure drop by 34.5%. The design with 5 total internal channels, comprised of 3 inlet channels and 2 outlet channels, attained a lower thermal resistance than the baseline design while reducing the pressure drop by 80.9%.

Figure 8 illustrates the effect of channels number on the maximum temperature and pressure drop of the heat sink. As the channel number increases, the maximum temperature increases due to the fact that fluid speed is decreased where heat transfer is aided by the fluid motion. The higher the speed, the greater the rate of heat transfer. This can be seen from the streamlines in Fig. 9, where for a smaller number of channels, the flow is almost equally distributed across the heat sink. However, when the number of channels increases, simulation results showed that the coolant did not penetrate ideally to the whole heated surface. As a result, lower heat capture ratios by the fluid as it passes through the heat sink, affect the heat sink's thermal performance. Increasing the number of channels minimizes the pressure drop over the heat sink for two main reasons. First, splitting the flow into several inlets rather than a single inlet decreases the flow speed in these inlets significantly. Second, the total distance traveled by the coolant inside the heat sink was reduced by shortening the path between the inlets and outlets.

To demonstrate the flow distribution inside the heat sink in greater detail, velocity streamlines for both the bassline and the 3 channels design are presented in Fig. 10. As noted in Fig. 10, looking at the fluid velocity through the channels of the heat sink, the 3 channels design has a lower fluid velocity than the baseline design, which explains the lower pressure drop in this design compared to the baseline. Moreover, the streamlines show that in this design the fluid was distributed more uniformly in the heat sink channels and penetrated de-eper, reaching the base of the fins. As a result, the heat transfer area increased, which subsequently enhanced convective heat transfer.

For the baseline and 3 internal channels designs, Fig. 11 depicts a side view of a resulting temperature plane located in the center of the heat sink. It is clear from this figure that the 3 internal channels design had a lower temperature for the fins and the chip compared to the baseline design. This is because before the fluid was removed, it

Table 6 Evaluated performance parameters for geometrical parametric study

Design	No. of inlets	No. of outlets	$w_{m,ch}$ (mm)	Flow rate (m^3/s) $\times 10^{-5}$	$T_{b,max}$ (°C)	R_{th} (°C/W)	ΔP (kpa)	COP (10^3)
Baseline	1	1	—	1.6667	56.4	0.061	2.23	10.8
3 channels	1	2	3.56	1.6667	53.9	0.0548	1.46	16.4
			3	1.6667	53.7	0.0543	1.541	15.6
			2	1.6667	53.8	0.0545	1.726	13.9
			1	1.6667	54.1	0.0553	2.286	10.5
			0.5	1.6667	54.1	0.0553	3.921	6.1
3 channels	2	1	3.56	1.6667	56.1	0.0603	1.36	17.7
			3	1.6667	55.8	0.0595	1.494	16.1
			2	1.6667	55.9	0.0598	1.6	15
			1	1.6667	56.1	0.0603	2.272	10.6
			0.5	1.6667	56.4	0.061	3.44	7
4 channels	2	2	3.56	1.6667	56.9	0.062	0.719	33.4
			3	1.6667	56.2	0.0605	0.754	31.8
			2	1.6667	56.1	0.0603	0.802	30
			1	1.6667	56.3	0.0608	1.129	21.3
			0.5	1.6667	57.4	0.0635	1.784	13.5
5 channels	2	3	3.56	1.6667	57	0.062	0.49	49
			3	1.6667	56.1	0.0603	0.506	47.4
			2	1.6667	55.2	0.058	0.552	43.5
			1	1.6667	55.8	0.0595	0.732	32.8
			0.5	1.6667	56.1	0.06025	1.169	20.5
5 channels	3	2	3.56	1.6667	55.9	0.0598	0.427	56.2
			3	1.6667	55.7	0.0593	0.524	45.8
			2	1.6667	55.9	0.0598	0.501	47.9
			1	1.6667	55.9	0.0598	0.651	36.9
			0.5	1.6667	55.7	0.0593	1.243	19.3
6 channels	3	3	3.56	1.6667	57.2	0.063	0.335	71.6
			3	1.6667	56.4	0.061	0.364	65.9
			2	1.6667	55.7	0.0593	0.405	59.3
			1	1.6667	55.7	0.0593	0.445	53.9
			0.5	1.6667	56.4	0.061	0.685	35
7 channels	3	4	3.56	1.6667	60.1	0.07	0.218	110
			3	1.6667	56	0.06	0.235	102.1
			2	1.6667	55.7	0.0593	0.24	100
			1	1.6667	55.4	0.0585	0.324	74
			0.5	1.6667	55.7	0.0593	0.561	42.8
7 channels	4	3	3.56	1.6667	59.9	0.068	0.219	109.6
			3	1.6667	56.4	0.061	0.227	105.7
			2	1.6667	56.1	0.0603	0.244	98.4
			1	1.6667	55.7	0.0593	0.345	69.5
			0.5	1.6667	56	0.06	0.595	40.3

traveled through the fins and reached the base of the fins. This significantly enhanced the heat transfer area and improved flow mixing, resulting in greater heat transfer coefficients.

To investigate the effect of flow rate variation on the performance of baseline and proposed designs, the flow rate was changed from 0.83×10^{-5} to 2.08×10^{-5} m^3/s (0.5 to 1.25 LPM) and the flow is laminar as Reynolds number range (334–834). A maximum flow rate of 1.25 LPM was selected to ensure that the speed of the fluid did not exceed 1.5 m/s in the heat sink channels, which would protect the heat sink fins from damage and corrosion [45]. With a flow rate above 1.25 LPM, the fluid speed would exceed the 1.5 m/s threshold in the baseline design. Figure 12 shows the R_{th}-Q, ΔP-Q, and COP curves for the proposed designs and the baseline design. Of all the flowrates investigated, the 3 channels design appeared to outperform the baseline design in terms of thermal resistance and pressure drop. Figure 12(*a*) illustrates the impact of flow rate on the thermal resistance of the different designs and as expected increasing the flow rate will increase the heat transfer coefficient and hence lower the thermal resistance. However, as the number of channels increases the thermal resistance increase because of having more channels means having lower fluid velocity and lower heat transfer coefficient. While Fig. 12(*b*) represents the pressure drop's relationship with flow rate. Note for the baseline design pressure drop increased significantly with the flow rate increased on the contradictory for the proposed designs. This shows the pressure drop was significantly reduced by increasing the number of internal channels, which was due to the lower fluid speed between the channels and the shorter flow path. Figure 12(*c*) illustrates that the lower pressure drop was

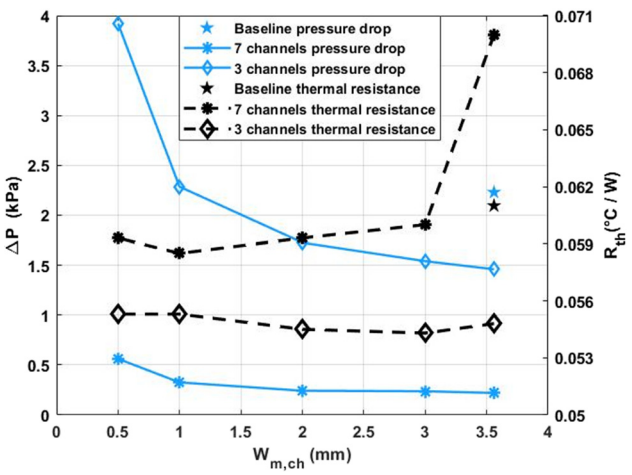

Fig. 13 Best designs comparison with baseline design

also reflected in the heat sink's COP, which showed a significant change in the pumping power between all the designs.

3.3 Parametric Study. A geometric parametric study was performed on the channel width to better understand how changing the width of the internally branched channels would impact the thermal resistance and pressure drop across the heat sink. Four different channel width values were considered: 3, 2, 1, and 0.5 mm. The length of the internal channels was kept constant at 30 mm. The calculated response parameters are listed in Table 6.

The table shows that channel width had less of an impact on thermal resistance for manifold designs with 4 channels or less. While for designs with 5 channels or more, decreasing channel width improved the thermal performance dramatically, which can be significantly observed in the 7 channels design where by reducing the channel width the maximum base temperature of the heat sink decreased by 4.7 °C from the original width. Moreover, decreasing the channel width resulted in an increase in the pressure drop, which was due to a rise in the fluid velocity through the channels of the heat sink. The 3 channels design was the best design while the 7 channels design was the most improved design in terms of thermal and hydraulic performance after the best design. As channel width was reduced, the degree of change in thermal resistance depended on the number of channels. For the 7 channels design, the thermal resistance decreased by a greater degree as channel width was reduced. For the 3 channels design, the thermal resistance decreased by a lesser degree as channel width was reduced. Based on this, thermal resistance became more sensitive to changes in channel width as the number of channels increased. As channel width was reduced, the degree of change in pressure drop also depended on the number of channels. The pressure drop increased as channel width decreased in both cases. However, its relationship with the number of channels was the reverse of thermal resistance's relationship with the number of channels. Pressure drop became less sensitive to changes in channel width as the number of channels increased. Figure 13 compares the best design, the most improved design, and the baseline design based on thermal resistance and pressure drop.

4 Conclusion

In this paper, several manifold designs were introduced, numerically investigated, and then compared with a commercially available cold plate. A numerical model was developed to evaluate the thermal resistance, pressure drop, and COP for the proposed designs. It was found that the manifold with 3 total channels, comprised of 1 inlet and 2 outlet internal channels, had the best performance with a thermal resistance of 0.054 °C/W, a pressure drop of 1.46 kPa, and a COP of 16.4×10^3. Afterward, a parametric study was conducted to identify the effect of manifold internal channel width on the thermal and hydraulic performance of the heat sink. It was found that changes in channel width had less of an impact on the thermal performance of a manifold with 4 or fewer channels and had a significant effect on pressure drop. However, for a manifold with 5 or more channels, it showed the reverse trend. with a significant decrease in thermal resistance accompanied by a little rise in pressure drop. The overall best design in terms of thermal performance was the 3 channels manifold with a 3 mm channel width, and the design with the most improvement after the best design was the manifold with 7 internal channels.

Acknowledgment

We would like to acknowledge Future Facilities Ltd. We would also like to thank the ES2 Partner Universities for their support and advice. This work is supported by NSF IUCRC Award No. IIP-1738793 and MRI Award No. CNS1040666.

Funding Data

- National Science Foundation (Funder ID: 10.13039/100000001).

Nomenclature

c_p = specific heat
$\dot{m}$ = mass flow rate
R_{th} = thermal resistance
k = thermal conductivity
P = pressure
T = temperature
u = velocity
Q = volumetric flow rate
q = total power
q'' = heat flux
ρ = fluid density
μ = dynamic viscosity
ΔP = pressure drop
CFD = computational fluid dynamics
COP = coefficient of performance
DC = data center
LPM = litter per minute
MPF = micro-pin fin

Subscripts

b = base
ch = channel
F = fins
f = fluid
in = inlet
m = manifold
out = outlet
s = solid

References

[1] Tradat, M. I., Manaserh, Y. "A., Sammakia, B. G., Hoang, C. H., and Alissa, H. A., 2021, "An Experimental and Numerical Investigation of Novel Solution for Energy Management Enhancement in Data Centers Using Underfloor Plenum Porous Obstructions," Appl. Energy, **289**, p. 116663.

[2] Manaserh, Y. M., Tradat, M. I., Bani-Hani, D., Alfallah, A., Sammakia, B. G., Nemati, K., and Seymour, M. J., 2022, "Machine Learning Assisted Development of IT Equipment Compact Models for Data Centers Energy Planning," Appl. Energy, **305**, p. 117846.

[3] Shehabi, A., Smith, S., Sartor, D., Brown, R., Herrlin, M., Koomey, J., Masanet, E., Horner, N., Azevedo, I., and Lintner, W., 2016, "United States Data Center Energy Usage Report," Lawrence Berkeley National Laboratory, Berkeley, CA, Report No. LBNL-1005775.

[4] Ma, Y., Ma, G., Zhang, S., and Xu, S., 2015, "Experimental Investigation on a Novel Integrated System of Vapor Compression and Pump-Driven Two Phase Loop for Energy Saving in Data Centers Cooling," Energy Convers. Manage., **106**, pp. 194–200.

[5] Manaserh, Y. M., Tradat, M. I., Gharaibeh, A. R., Sammakia, B. G., and Tipton, R., 2021, "Shifting to Energy Efficient Hybrid Cooled Data Centers Using Novel Embedded Floor Tiles Heat Exchangers," Energy Convers. Manage., **247**, p. 114762.

[6] Sauciuc, L., Chrysler, G., Mahajan, R., and Szleper, M., 2003, "Air-Cooling Extension-Performance Limits for Processor Cooling Applications," Ninteenth Annual IEEE Semiconductor Thermal Measurement and Management Symposium, San Jose, CA, Mar. 11–13, pp. 74–81.

[7] Broughton, J., Smet, V., Tummala, R. R., and Joshi, Y. K., 2018, "Review of Thermal Packaging Technologies for Automotive Power Electronics for Traction Purposes," ASME J. Electron. Packag., **140**(4), p. 040801.

[8] Zhang, H. Y., Pinjala, D., and Teo, P.-S., 2003, "Thermal Management of High Power Dissipation Electronic Packages: From Air Cooling to Liquid Cooling," Proceedings of the 5th Electronics Packaging Technology Conference (EPTC 2003), Singapore, Dec. 12, pp. 620–625.

[9] Asadi, M., Xie, G., and Sunden, B., 2014, "A Review of Heat Transfer and Pressure Drop Characteristics of Single and Two-Phase Microchannels," Int. J. Heat Mass Transfer, **79**, pp. 34–53.

[10] Hoang, C. H., Fallahtafti, N., Rangarajan, S., Gharaibeh, A., Hadad, Y., Arvin, C., Sikka, K., Schiffres, S. N., and Sammakia, B., 2021, "Impact of Fin Geometry and Surface Roughness on Performance of an Impingement Two-Phase Cooling Heat Sink," Appl. Therm. Eng., **198**, p. 117453.

[11] Sung, M. K., and Mudawar, I., 2009, "Single-Phase and Two-Phase Hybrid Cooling Schemes for High-Heat-Flux Thermal Management of Defense Electronics," ASME J. Electron. Packag., **131**(2), p. 021013.
[12] Kheirabadi, A. C., and Groulx, D., 2018, "Experimental Evaluation of a Thermal Contact Liquid Cooling System for Server Electronics," Appl. Therm. Eng., **129**, pp. 1010–1025.
[13] Marcinichen, J. B., Wu, D., Paredes, S., Thome, J. R., and Michel, B., 2014, "Dynamic Flow Control and Performance Comparison of Different Concepts of Two-Phase on-Chip Cooling Cycles," Appl. Energy, **114**, pp. 179–191.
[14] Bansode, P. V., Shah, J. M., Gupta, G., Agonafer, D., Patel, H., Roe, D., and Tufty, R., 2020, "Measurement of the Thermal Performance of a Custom-Build Single-Phase Immersion Cooled Server at Various High and Low Temperatures for Prolonged Time," ASME J. Electron. Packag., **142**(1), p. 011010.
[15] Shah, J. M., Padmanaban, K., Singh, H., Duraisamy Asokan, S., Saini, S., and Agonafer, D., 2021, "Evaluating the Reliability of Passive Server Components for Single-Phase Immersion Cooling," ASME J. Electron. Packag., **144**(2), p. 021109.
[16] Jalili, M., Manousakis, I., Goiri, Í., Misra, P. A., Raniwala, A., Alissa, H., Ramakrishnan, B., Tuma, P., Belady, C., Fontoura, M., and Bianchini, R., 2021, "Cost-Efficient Overclocking in Immersion-Cooled Datacenters," 2021 ACM/IEEE 48th Annual International Symposium on Computer Architecture (ISCA), Valencia, Spain, June 14–18, pp. 623–636.
[17] Tuckerman, D. B., and Pease, R. F. W., 1981, "High-Performance Heat Sinking for VLSI," IEEE Electron Device Lett., **2**(5), pp. 126–129.
[18] Gullbrand, J., Luckeroth, M. J., Sprenger, M. E., and Winkel, C., 2019, "Liquid Cooling of Compute System," ASME J. Electron. Packag., **141**(1), p. 010802.
[19] Lee, P.-S., Garimella, S. V., and Liu, D., 2005, "Investigation of Heat Transfer in Rectangular Microchannels," Int. J. Heat Mass Transfer, **48**(9), pp. 1688–1704.
[20] Kandlikar, S. G., and Bapat, A. V., 2007, "Evaluation of Jet Impingement, Spray and Microchannel Chip Cooling Options for High Heat Flux Removal," Heat Transfer Eng., **28**(11), pp. 911–923.
[21] Ndao, S., Peles, Y., and Jensen, M. K., 2014, "Effects of Pin Fin Shape and Configuration on the Single-Phase Heat Transfer Characteristics of Jet Impingement on Micro Pin Fins," Int. J. Heat Mass Transfer, **70**, pp. 856–863.
[22] Gupta, D., Saha, P., and Roy, S., 2021, "Computational Analysis of Perforation Effect on the Thermo-Hydraulic Performance of Micro Pin-Fin Heat Sink," Int. J. Therm. Sci., **163**, p. 106857.
[23] Siu-Ho, A., Qu, W., and Pfefferkorn, F., 2007, "Experimental Study of Pressure Drop and Heat Transfer in a Single-Phase Micropin-Fin Heat Sink," ASME J. Electron. Packag., **129**(4), pp. 479–487.
[24] Ahmadian-Elmi, M., Mashayekhi, A., Nourazar, S. S., and Vafai, K., 2021, "A Comprehensive Study on Parametric Optimization of the Pin-Fin Heat Sink to Improve Its Thermal and Hydraulic Characteristics," Int. J. Heat Mass Transfer, **180**, p. 121797.
[25] Li, Y., Wang, Z., Yang, J., and Liu, H., 2020, "Thermal and Hydraulic Characteristics of Microchannel Heat Sinks With Cavities and Fins Based on Field Synergy and Thermodynamic Analysis," Appl. Therm. Eng., **175**, p. 115348.
[26] Hasan, M. I., 2014, "Investigation of Flow and Heat Transfer Characteristics in Micro Pin Fin Heat Sink With Nanofluid," Appl. Therm. Eng., **63**(2), pp. 598–607.
[27] Ahmed, H. E., and Ahmed, M. I., 2015, "Optimum Thermal Design of Triangular, Trapezoidal and Rectangular Grooved Microchannel Heat Sinks," Int. Commun. Heat Mass Transfer, **66**, pp. 47–57.
[28] Wan, Z., and Joshi, Y., 2017, "Pressure Drop and Heat Transfer Characteristics of Pin Fin Enhanced Microgaps in Single Phase Microfluidic Cooling," Int. J. Heat Mass Transfer, **115**, pp. 115–126.
[29] Chiu, H.-C., Hsieh, R.-H., Wang, K., Jang, J.-H., and Yu, C.-R., 2017, "The Heat Transfer Characteristics of Liquid Cooling Heat Sink With Micro Pin Fins," Int. Commun. Heat Mass Transfer, **86**, pp. 174–180.
[30] Wiriyasart, S., and Naphon, P., 2019, "Liquid Impingement Cooling of Cold Plate Heat Sink With Different Fin Configurations: High Heat Flux Applications," Int. J. Heat Mass Transfer, **140**, pp. 281–292.
[31] Ryu, J. H., Choi, D. H., and Kim, S. J., 2003, "Three-Dimensional Numerical Optimization of a Manifold Microchannel Heat Sink," Int. J. Heat Mass Transfer, **46**(9), pp. 1553–1562.
[32] Boteler, L., Jankowski, N., McCluskey, P., and Morgan, B., 2012, "Numerical Investigation and Sensitivity Analysis of Manifold Microchannel Coolers," Int. J. Heat Mass Transfer, **55**(25–26), pp. 7698–7708.
[33] Whitt, R., Hudson, S., Huitink, D., Yuan, Z., Emon, A., and Luo, F., 2020, "Additive Manufactured Impinging Coolant, Low Electromagnetic Interference, and Nonmetallic Heat Spreader: Design and Optimization," ASME J. Electron. Packag., **142**(4), p. 041004.
[34] Zhou, F., Dede, E. M., and Joshi, S. N., 2015, "A Novel Design of Hybrid Slot Jet and Mini-Channel Cold Plate for Electronics Cooling," 2015 31st Thermal Measurement, Modeling & Management Symposium (SEMI-THERM), San Jose, CA, Mar. 15–19, pp. 60–67.
[35] Solovitz, S. A., and Mainka, J., 2011, "Manifold Design for Micro-Channel Cooling With Uniform Flow Distribution," ASME J. Fluids Eng., **133**(5), p. 051103.
[36] Wei, T. W., Oprins, H., Cherman, V., Beyne, E., and Baelmans, M., 2020, "Experimental and Numerical Investigation of Direct Liquid Jet Impinging Cooling Using 3D Printed Manifolds on Lidded and Lidless Packages for 2.5 D Integrated Systems," Appl. Therm. Eng., **164**, p. 114535.
[37] Gonzalez-Valle, C. U., Samir, S., and Ramos-Alvarado, B., 2020, "Experimental Investigation of the Cooling Performance of 3-D Printed Hybrid Water-Cooled Heat Sinks," Appl. Therm. Eng., **168**, p. 114823.
[38] Jung, K. W., Cho, E., Lee, H., Kharangate, C., Zhou, F., Asheghi, M., Dede, E. M., and Goodson, K. E., 2020, "Thermal and Manufacturing Design Considerations for Silicon-Based Embedded Microchannel-3D Manifold Coolers (EMMCs): Part 1—Experimental Study of Single-Phase Cooling Performance With R-245fa," ASME J. Electron. Packag., **142**(3), p. 031117.
[39] Jung, K. W., Hazra, S., Kwon, H., Piazza, A., Jih, E., Asheghi, M., Gupta, M. P., Degner, M., and Goodson, K. E., 2020, "Thermal and Manufacturing Design Considerations for Silicon-Based Embedded Microchannel-Three-Dimensional Manifold Coolers—Part 2: Parametric Study of EMMCs for High Heat Flux ($\sim$1 kW/cm^2) Power Electronics Cooling," ASME J. Electron. Packag., **142**(3), p. 031117.
[40] Zhou, J., Chen, X., Zhao, Q., Lu, M., Hu, D., and Li, Q., 2021, "Flow Thermohydraulic Characterization of Hierarchical-Manifold Microchannel Heat Sink With Uniform Flow Distribution," Appl. Therm. Eng., **198**, p. 117510.
[41] Luo, Y., Zhang, J., and Li, W., 2020, "A Comparative Numerical Study on Two-Phase Boiling Fluid Flow and Heat Transfer in the Microchannel Heat Sink With Different Manifold Arrangements," Int. J. Heat Mass Transfer, **156**, p. 119864.
[42] Zhou, F., Liu, Y., Liu, Y., Joshi, S. N., and Dede, E. M., 2016, "Modular Design for a Single-Phase Manifold Mini/Microchannel Cold Plate," ASME J. Therm. Sci. Eng. Appl., **8**(2), p. 021010.
[43] Gilmore, N., Timchenko, V., and Menictas, C., 2020, "Open Manifold Microchannel Heat Sink for High Heat Flux Electronic Cooling With a Reduced Pressure Drop," Int. J. Heat Mass Transfer, **163**, p. 120395.
[44] Gharaibeh, A. R., Tradat, M. I., Rangarajan, S., Sammakia, B. G., and Alissa, H. A., 2022, "Multi-Objective Optimization of 3D Printed Liquid Cooled Heat Sink With Guide Vanes for Targeting Hotspots in High Heat Flux Electronics," Int. J. Heat Mass Transfer, **184**, p. 122287.
[45] Myers, J., and Cohen, A., 2005, "Copper-Tube Corrosion in Domestic Water Systems," HPAC Eng., **77**(6), pp. 22–31.